1
2
3
4
5
6
7
8
9
10
11
12
13
14
15
16
17
18
19
20
21
22
23
24
25
26
27
28
29
30
31
...

Plasma Thermal-Chemical Instability of Low-Temperature Dimethyl Ether Oxidation in a Nanosecond-Pulsed Dielectric Barrier Discharge

Hongtao Zhong[1], Xin Yang[2,3], Xingqian Mao[1], Mikhail N. Shneider[1], Igor V. Adamovich[2] and Yiguang Ju[1]

[1]Department of Mechanical and Aerospace Engineering, Princeton University, Princeton, NJ 08544, US

[2]Michael A. Chaszeyka Nonequilibrium Thermodynamics Laboratory, The Ohio State University, Columbus, OH 43210, US

[3]State Key Laboratory of Electrical Insulation and Power Equipment, Xi'an Jiaotong University, Xi'an, 710049, PRC

E-mail: hongtaoz@princeton.edu

June, 2022

Abstract.

Plasma stability in reactive mixtures is critical for various applications from plasma-assisted combustion to gas conversion. To generate stable and uniform plasmas and control the transition towards filamentation, the underlying physics and chemistry need a further look. This work investigates the plasma thermal-chemical instability triggered by dimethyl-ether (DME) low-temperature oxidation in a repetitive nanosecond pulsed dielectric barrier discharge. First, a plasma-combustion kinetic mechanism of DME/air is developed and validated using temperature and ignition delay time measurements in quasi-uniform plasmas. Then the multi-stage dynamics of thermal-chemical instability is experimentally explored: the DME/air discharge was initially uniform, then contracted to filaments, and finally became uniform again before ignition. By performing chemistry modeling and analyzing the local thermal balance, it is found that such nonlinear development of the thermal-chemical instability is controlled by the competition between plasma-enhanced low-temperature heat release and the increasing thermal diffusion at higher temperature. Further thermal-chemical mode analysis identifies the chemical origin of this instability as DME low-temperature chemistry. This work connects experiment measurements with theoretical analysis of plasma thermal-chemical instability and sheds light on future chemical control of the plasma uniformity.

Submitted to: *Plasma Sources Sci. Technol.*

Plasma Thermal-Chemical Instability 2

1. Introduction

Following the global transitions to carbon-neutral energy economy, the increasing availability of renewable electricity provides a unique opportunity to reform fossil fuels into value-added chemicals and materials based on non-equilibrium plasma discharges [1, 2]. In addition, to develop advanced combustion and propulsion technologies, it is critical to control flow and reaction progress by manipulating discharge or plasma properties [3–6]. For these applications, volumetric and stable weakly ionized plasmas are desired to meet high efficiency, chemical reactivity and selectivity. However, the plasma volume in many cases is vulnerable to perturbations and generates local "hot spots". It is of great importance to understand the mechanism of plasma instabilities and pattern formation in the chemically reactive flow.

Studies of instabilities in weakly ionized plasma could be traced back to 1960s [7–10]. Most of the work focused on noble gases and gas laser mixtures. Several underlying mechanisms including the well-known thermal-ionization instability [9] were identified and discussed in great details. The thermal-ionization mechanism qualitatively can be described as follows: if the local electron number density n_e is perturbed, and such fluctuation can not be dissipated effectively, Joule heating (directly proportional to n_e) raises the local temperature, leading to the thermal expansion (gas number density $N \downarrow$), higher local reduced electric filed ($E/N \uparrow$), and an enhanced electron-impact ionization rate. Faster ionization further increases n_e. Recently, more attention goes to the thermal-chemical instability in reactive and combustible mixtures [11–13]. Such instability is proposed to address the positive feedback and couplings between discharge non-uniformity and plasma-enhanced chemical reactions. Under such hypothesis, Zhong *et al* [11] numerically studied the dynamic contraction in a fuel-lean $H_2/O_2/N_2$ mixture with a simplified plasma-combustion kinetic mechanism. The results showed that the critical conditions of contraction in a DC discharge were modified by the elementary reactions of hydrogen combustion. The thermal-chemical mode analysis [12] revealed that dynamic contraction and chemical kinetics interact in a variety of time scales from millisecond to sub-microsecond. Moreover, kinetic pathways including fuel oxidation by vibrational and electronically excited species are critical for destabilizing such DC discharges.

In experiments, studies of plasma-assisted ignition of hydrocarbon-air mixtures [14–16] and hydrogen–air mixtures [17, 18] in repetitive nanosecond pulsed discharges clearly showed that the filamentation in reactive mixtures developed faster than that in air. Several strategies to improve the plasma uniformity were developed including preheating the gas, manipulating the voltage waveform, increasing convection or using different bath gases [19, 20]. While these experimental studies provide practical guidelines of controlling plasma thermal-chemical instability, quantitative diagnostics to investigate the mechanism was limited. More recently, Rousso *et al* [13] performed high-speed imaging for instability development in $CH_4/O_2/Ar$ mixtures and measured one-dimensional time-resolved electric field strengths. They concluded that

Plasma Thermal-Chemical Instability 3

the occurrence of the thermal-chemical instability changed the plasma properties by forming multiple secondary discharges and possibly led to micron-sized non-uniform electric field distributions. Other recent experimental studies for thermal-chemical instability focused more on its applications including plasma-assisted CO_2 conversion or N_2 fixation processes in microwave plasmas [21–23]. The modeling suggested that thermal chemistry played a major role in contraction dynamics. Nevertheless, many fuel and chemicals have low temperature chemistry (LTC) below 1000 K. The LTC reaction pathways are different from those of high temperature chemistry. Therefore, it is necessary to understand the plasma thermal-chemical instability with LTC.

In this work, we aim to study the plasma thermal-chemical instability in dimethyl ether (DME)/air mixtures in repetitive nanosecond pulsed dielectric barrier discharges (DBD). Nanosecond pulsed discharges are known for generating high spatial uniformity in air plasmas, even with boundary and initial conditions of low-amplitude disturbances from the discharge or flows [24]. Nanosecond pulsed discharges may exclude other instability mechanisms than the targeted thermal-chemical effects. DME is chosen as the fuel for two reasons. Firstly, it has been proposed as a future alternative fuel for its remarkable auto-ignition characteristics and low levels of soot emissions [25–27]. Understanding plasma instabilities in DME mixtures may facilitate future plasma-assisted fuel reforming and ignition studies. Secondly, compared to methane or hydrogen, DME exhibits a two-stage ignition mode due to its LTC effect [28, 29]. Previous studies of plasma-assisted DME oxidation [25–27, 30–32] already showed that plasmas could efficiently produce chemically active species and greatly modify the kinetic pathways of DME oxidation. Such a strong low temperature reactivity in DME mixtures may be coupled with plasma filamentation far below the ignition threshold.

The objective of this work is twofold: first, to provide direct proof of plasma thermal-chemical instability controlled by DME low-temperature chemistry; second, to present possible key low-temperature kinetic pathways for triggering such instability. The paper is structured as the followings: In Section 2 and 3, experimental setup, numerical models and analysis methods are introduced. In Section 4.1, a DME/air plasma-assisted combustion kinetic mechanism is developed and validated against time-resolved temperature and ignition delay measurements in quasi-uniform plasmas. This chemical mechanism is the key for analyzing the plasma thermal-chemical instability. In Section 4.2, time-resolved single-shot ICCD imaging for DME-air and air mixtures during the plasma thermal-chemical instability is presented. Qualitatively, such imaging provides how filamentation forms and dissipates with respect to pulse numbers in different compositions. A local thermal balance is performed to estimate the number of pulses required for instability development. DME low-temperature heat release and thermal diffusion are considered as major stabilization/destabilization sources. Finally, in Section 4.3, thermal-chemical mode analysis (TCMA) is performed to further inspect the chemical origin of this plasma instability. The evolution of unstable chemical modes are resolved and relevant plasma-assisted low-temperature fuel oxidation reactions contributing to the plasma instability are identified.
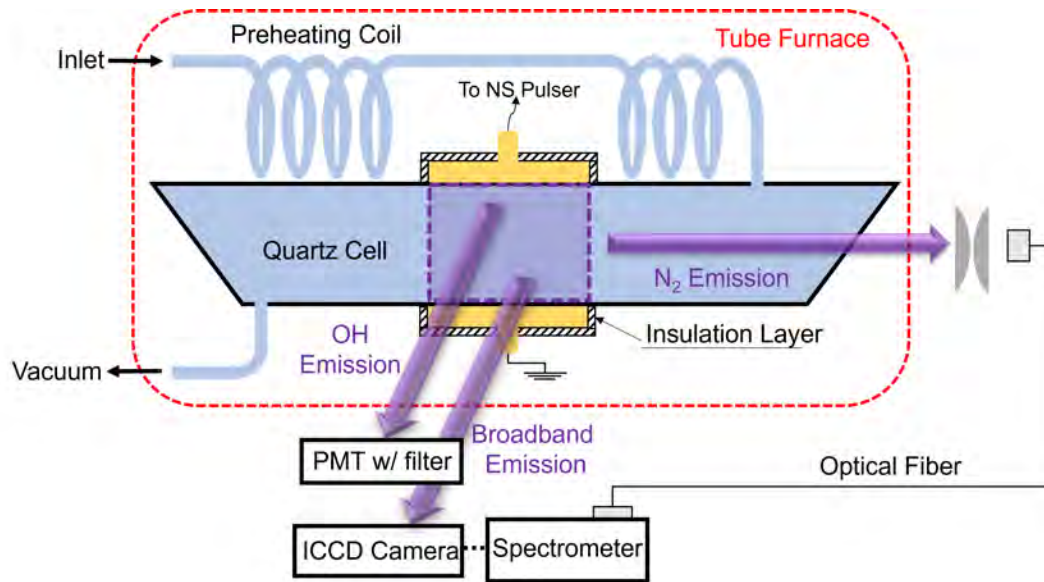
2. Experimental

Figure 1: Experimental setup. Plasma emissions are either measured parallel with the flow (stream-wise), or perpendicular to the flow (orthogonal).

The schematic of the experimental setup is shown in Fig. 1 and reported in previous studies [17, 18]. The reactor consists of a 280-mm-long, 22 mm × 10 mm rectangular cross-sectional quartz channel with a wall thickness of 1.75 mm. Two 1-mm-thick planar quartz windows are fused to the two ends at Brewster's angle, providing optical access in the stream-wise direction. The gas stream and the entire discharge cell are placed inside a tube furnace (Thermcraft, Ltd). A 1-m-long quartz tube coil, fused to the surface of the quartz channel, serves as a preheating inlet. The temperature of the discharge section can be preheated up to 850 K. The furnace temperature (outside the flow channel) is monitored by a thermocouple. Without any plasma discharge, extra thermocouples have been inserted to different positions of the channel to verify the temperature uniformity with and without the flow. The difference between the furnace temperature and the actual flow temperature in the channel is within 5K over a wide temperature range.

DME flow (Praxair, 99.5%) through the cell is regulated by a choked sonic orifice (Swagelok), used as a flow meter. The flow rates are calibrated using a pressure gauge (Cecomp Electronics). Air flow rates are controlled by the MKS mass flow controller. Fuel and air flows are premixed before entering the cell. The cell pressure is kept at 100 Torr. The initial temperatures are varied from room temperature (300 K) to 600 K. The molar fraction of DME is adjusted from 3% to 13% and the equivalence ratios Φ are from 0.4 to 2.1. The total flow rate is 1000 sccm and the corresponding residence time of the flow in the discharge is ~ 0.05 s.

Two rectangular stainless-steel plate electrodes, 14 mm × 60 mm each, are placed

Plasma Thermal-Chemical Instability   5

on the top and bottom of the channel halfway between the ends and are held in place by ceramic clamps. The electrodes are covered by the macor ceramic plates. Such insulation is necessary to prevent corona discharge formation and reduce the energy loss outside the reactor. The electrodes are connected to the MegaImpulse pulse generator (NPG-18/100k, peak voltage up to 36 kV, pulse duration of 5-10 ns FWHM, repetition rate up to 100 kHz). In the present work, the pulser is operated in repetitive burst mode, producing bursts of up to 400 pulses at a pulse repetition rate of 10 kHz and a burst repetition rate from single-shot to 1 Hz. A typical voltage waveform is provided in the Supplementary material.

Single-shot broadband plasma emission images are taken using a gated ICCD camera (Princeton Instruments PIMAX-4 1024i) with a UV lens (UV-Nikkor 105 mm f/4.5, Nikon) using a 500 ns gate. For ignition and flame propagation images after the discharge bursts, the gate time is 200 μs. The camera is triggered by a delay/pulse generator (SRS DG535). Ignition is also confirmed by monitoring time-resolved OH emissions from the discharge section using a band-pass filter centered at 310 ± 2 nm, a gated photomultiplier tube (PMT, Hamamastu Photonics, R3896), and a digital oscilloscope (LeCroy Waverunner MXi-A).

The time-resolved rotational temperature in the plasma during the pulse burst is inferred by fitting the N$_2$ C$^3\Pi_u \longrightarrow$ B$^3\Pi_u$ (v$' = 0$, v$'' = 0$) band emission to synthetic spectra, using the methods described in [33]. The optical emission spectroscopy (OES) setup consists of a spectrometer (Acton Research SpectraPro 2500i spectrometer, 2400-g/mm grating) and a gated PI-MAX ICCD camera. The OES temperature measurements are only made in the case of quasi-uniform plasmas. Emissions were collected from the end view, passing through a UV-Visible optical fiber (Ocean Optics) and then focused into the spectrometer. A 1-μs-gate is set on the ICCD camera to only collect emissions during a single discharge pulse to exclude other possible mechanisms exciting N$_2$ C$^3\Pi_u$ in the afterglow of the discharge [34]. Calibration experiments are performed to determine the uncertainty of the method: the flowing air with a flow rate of 100 sccm is first heated, reaching a steady-state temperature T_0. T_0 is confirmed by the furnace thermocouple. Then 10 nanosecond discharge pulses are fired to provide optical emissions. The emission spectrum near 337 nm at the tenth pulse is measured and fitted to infer the gas temperature in the plasma. Since 10 pulses in air will not increase the temperature significantly [35], the comparison between the OES-inferred temperature and the thermocouple-measured temperature will illustrate the accuracy of the OES measurements. We varied T_0 from room temperature (300 K) to 850 K. The uncertainty varies with T_0 and is up to 50 K. The calibration details are provided in the Supplementary material. To improve signal-to-noise ratio, the emission spectra are averaged over 500 measurement shots.

3. Nanosecond Pulsed DBD Discharge Model and Plasma-Assisted DME/O$_2$/N$_2$ Mechanism

A nanosecond pulsed DBD discharge model is developed following [12, 15, 36]. The governing equation for species number density (N_i) and gas temperature (T) is written in a general form (the operator D/Dt is material time derivative) as

$$\frac{DN_i}{Dt} = \sum_{j=1}^{j_{max}} \omega_{ij}(t) + \nabla\left[D_i(T)\nabla N_i\right] \quad (i=1,2,3,\cdots,i_{max}) \tag{1}$$

$$\rho c_p \frac{DT}{Dt} = q_{coupled}\nu_{rep} - \frac{3}{2}\frac{\partial(n_e k_B T_e)}{\partial t} - \sum_i^{i_{max}} h_i \frac{\partial N_i}{\partial t} + \nabla\left[\lambda(T)\nabla T\right] \tag{2}$$

where i is the species index in the chemical mechanism and N_i is the number density of species i. ω_{ij} is production or consumption rate of species i contributed by reaction j. $D_i(T)$ is diffusivity of species i. i_{max} and j_{max} are the total numbers of species and reactions in the chemical mechanism. In Eqn (2), ρ is the gas density and $c_p(T)$ is the specific heat. $q_{coupled}$ is the coupled pulse energy, ν_{rep} is the pulse repetition rate in a burst, k_B is the Boltzman constant, and T_e is the effective electron temperature (unit: K). h_i are enthalpies of chemical and excited species. $\lambda(T)$ is the thermal conductivity. In the current model, we only consider the transition in the bulk plasma volume. The plasma sheath layers are not discussed or modelled. Physically, it provides the initial destabilization to the plasma volume.

The gap voltage V_{gap} is connected to the applied voltage V_{app} through [37]

$$\frac{dV_{app}(t)}{dt} = \left(1 + \frac{2l}{\varepsilon L}\right)\frac{dV_{gap}(t)}{dt} + \frac{2lq_e}{\varepsilon_0\varepsilon}\frac{1}{L} \times \int_0^L \left[\Gamma_+(x,t) - \Gamma_e(x,t)\right] dx \tag{3}$$

where $V_{app}(t)$ is the applied voltage measured with the voltage probe (Tektronix P6015A). q_e is the elementary charge and ε is the dielectric constant, and L and l are the discharge gap and the dielectric plate thickness. Γ_+ and Γ_e are the drift-diffusion fluxes for ions and electrons. Eqn (3) describes gap voltage reduction during the pulse due to charge accumulation on surfaces of the dielectric plates. The parameters used in the model are assumed to be the same as in the experiments: gap distance $L = 1$ cm, dielectric layer thickness $l = 1.75$ mm, and plasma volume $A = 8.4$ cm^3, with the dielectric constant of quartz $\varepsilon = 3.8$.

In the case of uniform plasma volumes, the spatial terms in Eqn (1) - (3) will vanish and the above system degenerate into a zero-dimensional system:

$$\frac{dN_i}{dt} = \sum_{j=1}^{j_{max}} \omega_{ij}(t) \quad (i=1,2,3,\cdots,i_{max}) \tag{4}$$

$$\rho c_p \frac{dT}{dt} = q_{coupled}\nu_{rep} - \frac{3}{2}\frac{d(n_e T_e)}{dt} - \sum_i^{i_{max}} h_i \frac{dN_i}{dt} \tag{5}$$

$$\frac{dV_{app}(t)}{dt} = \left(1 + \frac{2l}{\varepsilon L}\right)\frac{dV_{gap}(t)}{dt} + \frac{2l}{\varepsilon_0\varepsilon}q_e n_e \mu_e E \tag{6}$$

In this work, the general form of the governing equation is not explicitly solved. As the focus of this work is chemical instability, zero-dimensional chemical kinetic calculations will provide great insights. In Sect 4.2, orders of magnitude for both spatial terms and chemical source terms will still be estimated, which will further emphasize the importance of the chemical kinetics.

The species and temperature evolutions (Eqn (4) - (6)) are solved numerically by incorporating the plasma kinetics solver ZDPlasKin [38] and the combustion kinetics solver CHEMKIN II [39] with a splitting scheme [40, 41]. The electron energy distribution function (EEDF) and the rate coefficients of electron-impact reactions are calculated by a Boltzmann equation library BOLSIG+ [42]. The cross sections of electron-impact reactions of N_2 and O_2 are obtained from Phelps database in the LXCat Project [43], while the cross section data for DME is from Magboltz database [44] (see Supplementary material). The corresponding electron-impact reactions of DME are included in Table 1.

Based on the above electron cross section data, fractional electron power dissipated into the different degrees of freedom in the air and typical DME/air mixtures are calculated and shown in Fig. 2. For both cases, below 100 Td, most of the electron energy goes to vibrational excitation while above 100 Td, electronic excitation, dissociation and ionization become more pronounced. With the addition of DME, more electron energy goes to ionization at around 100 Td. Also electron-impact DME dissociation at higher E/N (above 100 Td) is non-negligible, leading to the active generation of radicals such as H and CH_3. At the present conditions, the peak reduced electric field from the calculation is $E/N = 350 - 700$ Td, which decays to zero at the end of a plasma pulse.
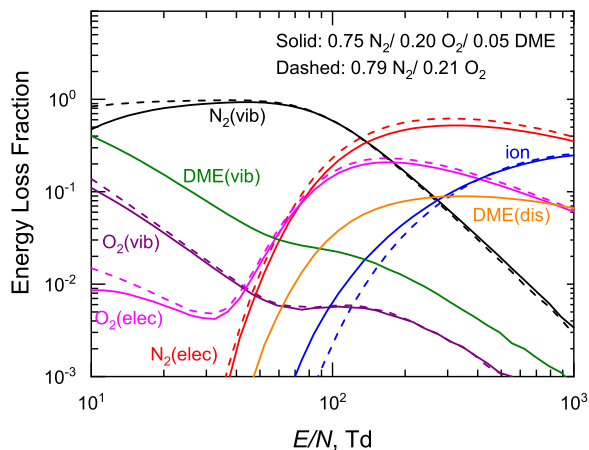

Figure 2: Fractional electron power dissipated into the different degrees of freedom in air and DME/air mixtures versus the reduced electric field E/N. The calculation is made by BOLSIG+. Gas temperature 300 K.

To model the kinetics of plasma-assisted DME oxidation, we develop a plasma-assisted $DME/N_2/O_2$ kinetic mechanism. Briefly, the model incorporates a non-equilibrium air plasma kinetic model and $DME/N_2/O_2$ combustion kinetic model. In

Plasma Thermal-Chemical Instability   8

Table 1: DME reactions with electrons/ions/excited N_2/O_2 species. (T_e is electron temperature in K).

Reaction	Rate constants, cm^3/s	Reference
$e + CH_3OCH_3 \longrightarrow e + e + CH_3OCH_3^+$	$k = f(E/N)$	[31]
$e + CH_3OCH_3 \longrightarrow e + CH_3OCH_3$ (ν = 1-5)	$k = f(E/N)$	[31]
$e + CH_3OCH_3 \longrightarrow e + CH_3OCH_2 + H$	$k = f(E/N)$	[31]
$e + CH_3OCH_3 \longrightarrow e + CH_3O + CH_3$	$k = f(E/N)$	[31]
$e + CH_3OCH_3^+ \longrightarrow O + CH_3 + CH_3$	$1.5 \times 10^{-7} \times (T_e/300)^{-0.5}$	[31]
$e + CH_3OCH_3^+ \longrightarrow CH_2O + CH_4$	$3.0 \times 10^{-7} \times (T_e/300)^{-0.5}$	[31]
$e + CH_3OCH_3^+ \longrightarrow CH_2 + CH_3OH$	$1.5 \times 10^{-7} \times (T_e/300)^{-0.5}$	[31]
$O(^1D) + CH_3OCH_3 \longrightarrow CH_2OH + CH_3O$	6.3×10^{-10}	[31]
$O_2^* + CH_3OCH_3 \longrightarrow O_2 + CH_3O + CH_3$	1.0×10^{-10}	[31]
$O_2(a1) + CH_3OCH_3 \longrightarrow O_2 + CH_3OCH_3$	$5.46 \times 10^{-10} \times exp(-5850/T_{gas})$	[26]
$O_2(a1) + CH_3OCH_3 \longrightarrow CH_3OCH_2 + HO_2$	$7.01 \times 10^{-11} \times exp(-17620/T_{gas})$	[26]
$O_2(b1) + CH_3OCH_3 \longrightarrow O_2(a1) + CH_3OCH_3$	1.08×10^{-13}	[26]
$N_2(A,B,a') + CH_3OCH_3 \longrightarrow N_2 + CH_3O + CH_3$	3.0×10^{-10}	estimated
$N_2(C) + CH_3OCH_3 \longrightarrow N_2 + CH_3O + CH_3$	5.0×10^{-10}	estimated

total 720 combustion reactions, 559 plasma reactions, and 112 species are considered. The plasma sub-model is based on previous studies [12]. 49 electron-impact processes are considered for the EEDF calculation. Due to the complexity of the non-equilibrium chemistry involving fuels, most of the plasma-assisted DME reactions remain unclear. DME reactions with excited species are listed in Table 1. The combustion sub-model is developed and validated in previous literature [29, 45, 46]. The model incorporates the sub-mechanisms of DME oxidition, NO_x formation, and NO_x couplings with hydrocarbons at low temperatures [47]. Detailed reactions and species are provided in the Supplementary material.

With the discharge model and the kinetic mechanism, thermal-chemical mode analysis (TCMA) are further performed to understand how chemistry influences the system stability. TCMA is a Jacobian-based analysis [12]. It originates from the computational singular perturbation (CSP) theory [48], developed by Lam and co-workers, which has been applied to understand various stability phenomena triggered by chemical kinetics. One example is the ignition/extinction of a combustible mixture. The Jacobian is defined as

$$\mathbf{J} = \frac{\partial \omega_s}{\partial \mathbf{y}} \tag{7}$$

$\mathbf{y}$ is the vector of variables. In this work $\mathbf{y}$ includes species number density and temperature. ω_s is the source term for the variable vector (the right-hand-side of Eqn

4 and 5). By calculating the eigenvalues of the time-dependent Jacobian matrix, i.e.,

$$\mathbf{J} = A\Lambda B \tag{8}$$

Λ is the diagonal matrix as diag(λ_1, λ_2, ...). A and B are composed of column and row eigenvectors $\mathbf{a_i}$ and $\mathbf{b_i}$, respectively. Essentially TCMA converts the system dynamics from the basis of individual species and temperature to different "thermal-chemical modes" (TCMs). Every mode can be represented by one eigenvalue λ_i. When the leading eigenvalue exceeds zero, i.e.,

$$max\ Re\left[\lambda(\mathbf{J})\right] > 0 \tag{9}$$

the system is chemically unstable or "explosive". The corresponding TCMs tend to grow exponentially with the time scale of λ_i^{-1}. If all eigenvalues are below zero, the system is reaching the chemical equilibrium as all TCMs will decay.

TCMA can further connect the system stability to specific species and reactions by using the same concept of radical pointer proposed by Lam in CSP. The "explosive mode species/temperature pointer" (SP) is defined as

$$SP_i = diag(\mathbf{a_i} \cdot \mathbf{b_i}) \quad i = 1, 2, \cdots, N \tag{10}$$

The kth entry of SP_i indicates the correlations between the kth variable in the column vector $\mathbf{y}$ and the ith TCM. The "representative active species" (RAS) for the chemical mode is defined as the species which has the largest SP values among all species. In other words, a certain TCM is mostly related to its RAS.

4. Results and Discussions

4.1. Validation of plasma-assisted DME/O₂/N₂ kinetic mechanism

At elevated temperatures, the plasma keeps good uniformity throughout the entire burst. Typical ICCD images are included in the Supplementary material. The quasi-uniform plasma provides a great platform to examine and validate the chemistry mechanism.

In this work, we measured the minimum number of discharge pulses necessary to ignite the flow during one discharge burst at 500 - 600 K. The OH ($A^2\Sigma \rightarrow X^2\Pi$) emission "footprints" are shown in Fig. 3 (a-c). It was observed that turning the plasma off right before ignition did not affect the subsequent ignition. As shown in Fig. 3(b), for example, when $T_0 = 550$ K, the discharge was turned off after 227 pulses (22.7 ms). Within the plasma burst, the discharge noise interfered with the UV emissions received by PMT. Nonetheless, it could be seen that OH emissions were maintained at a low level before the end of the discharge. The ignition onset time was estimated as 0.3 ms after the burst was turned off. The UV emissions are consistent with ICCD images of the flame dynamics (camera gate of 200 μs), shown in Fig. 3(d). At 0.5 ms, there were two autoignition kernels in the downstream of the discharged region. One flame kernel propagated downstream and disappeared in the field of view. The other

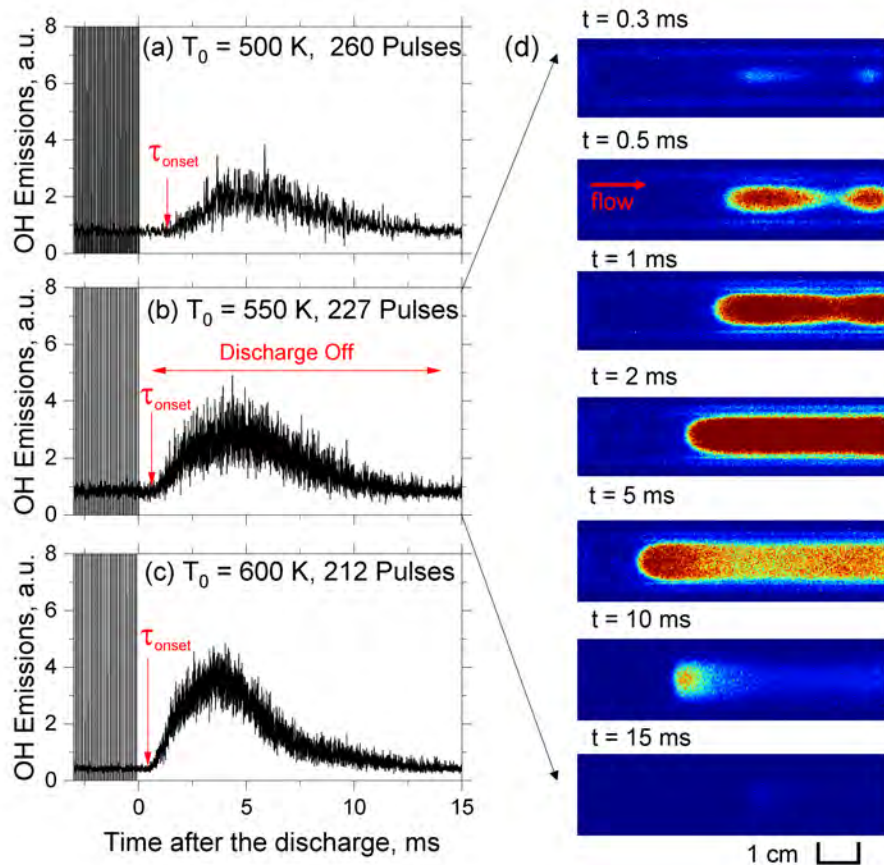*Plasma Thermal-Chemical Instability* 　　　　　　　　　　　　　　　　　10

Figure 3: Left (a,b,c): Time-resolved UV emission (310 nm) from a 5% DME/air mixture during ignition by a repetitive nanosecond pulsed discharge burst. Red arrows indicate the time when OH emissions start to rise (OH onset time). The initial temperature T_0 = 500, 550, and 600 K. P = 100 Torr. ν = 10 kHz. Right (d): ICCD camera images of the flame propagation. The flow direction is labeled. T_0 = 550 K.

one first propagated upstream. Eventually the inflow of the fresh mixture quenched the auto-ignition.

In Fig. 4, the ignition delay time (IDT) predicted by the discharge model and chemistry mechanism is further compared with experimental measurements. In the model, IDT is determined from peak OH concentration. In the experiment, IDT is determined from OH onset time as discussed above. At low pressures, the NTC effect in the DME auto-ignition is less prominent. By applying the plasma discharge and considering the energy coupling, IDT is reduced by orders of magnitude and the NTC effect is even diminished. The model correctly captures the trend of ignition delay time reduction as the initial temperature is increased from 500 K to 600 K. For each temperature, optical emission spectra of the plasma (partially rotationally resolved $0 \rightarrow 2$ band of the N_2 $C^3\Pi_u \longrightarrow B^3\Pi_u$ band system) have been recorded to infer the rotational temperature in the quasi-uniform plasma right at the beginning of the discharges and right before the ignition. The OES data provide another validation targets for the DME-

Plasma Thermal-Chemical Instability   11

air chemistry mechanism. The results show a reasonable match for the temperature rise. The disagreement between the model prediction and the measured data is about $\sim$15 %, which may be caused by the uncertainty of the reaction rates in the mechanism, multi-dimensional flow geometry, and the errors introduced by the plasma interference during the OES measurements. Certainly quantitative time-resolved species measurements are needed to further verify the correctness of the mechanism, which are beyond the scope of the current work.

From the simulated temperature profile, a two-stage temperature rise is clear, which is controlled by the plasma-assisted low-temperature chemistry (LTC). In the homogeneous auto-ignition, an isothermal period typically exists between the first and the second stage ignition. However, in the plasma-assisted ignition, energy deposition from the discharge helps to accelerate the chain branching process, overcome the isothermal stage, and connect the two-stage ignition within the millisecond time scale.

In summary, LTC at this low-pressure condition is accessible through the plasma activation. The zero-dimensional model can predict the temperature rise and the subsequent ignition phenomena. In return, LTC is expected to provide destabilization sources and create new dynamics for the plasma discharge.
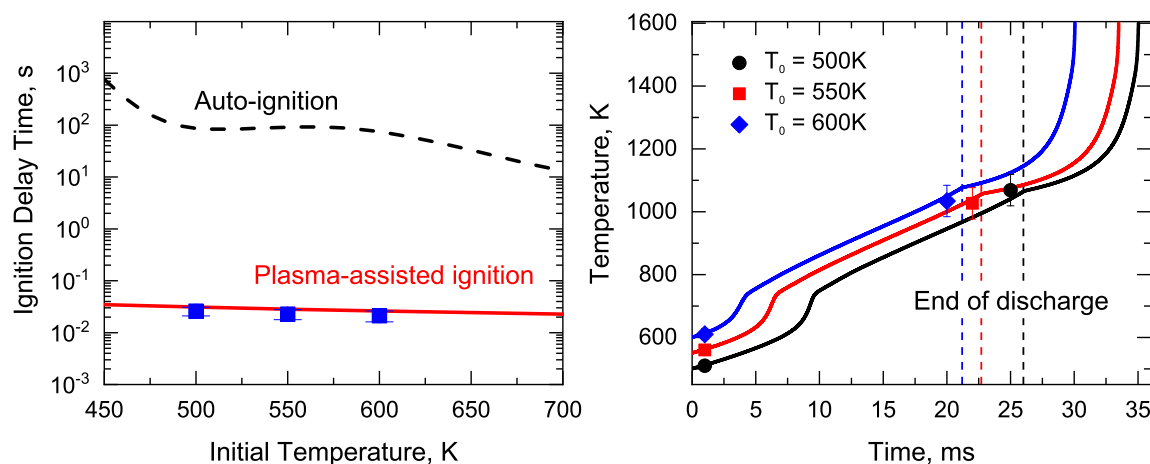

Figure 4: Left: Ignition delay times for DME/air = 5/95 at p = 100 Torr, T_0 = 450 - 700 K. Black dashed lines correspond to autoignition without plasma effects. Red solid lines correspond to homogeneous ignition using the current repetitive nanosecond pulsed DBD discharge model. Blue points indicate the ignition delay measurements using OH emissions. Right: Comparison of the model output and the OES temperature measurements. The measurements are made at pulse 20 and the pulse right before the ignition.

4.2. Imaging and analysis of thermal-chemical instability triggered by DME low-temperature oxidation

With validated plasma-assisted low-temperature DME oxidation mechanism, in this section the coupling between plasma instability and low-temperature fuel oxidation kinetics is further discussed.

Fig. 5 shows the comparison of the broad-band ICCD images taken in air and DME/air plasmas at an ambient temperature of 400 K. Throughout the burst, the uniformity along the flow direction is ensured in the center of the air plasma. The non-uniformity on the sides tends to be reproducible across different pulses and bursts. Thus, we conclude that these are likely caused by plasma edge effects (the electrode edge is indicated in the figure) rather than the target thermal-chemical instability. For the remainder of this work, these edge formations will not be discussed. For comparison, the air plasma mixed with 5% DME remains uniform at pulse 10 and 20. Then multiple well-defined filaments are formed from pulse 40 to 150. Interestingly after 150 pulse, however, these filaments become less pronounced and the plasma returns to the uniform state. At pulse 363, flame kernels are clearly observed and propagate in the reactor.

To understand nonlinear effects of the DME fuel chemistry on the plasma instability, first we applied OES to measure the temperature at pulse 20 and pulse 200, where the quasi-uniform assumption holds for both air and DME/air mixtures. At pulse 20, the temperature difference is within the maximum OES experimental uncertainty of 50 K (The sample spectra are provided in Supplementary material). Both air and DME/air plasmas maintain good uniformity to this point. At pulse 200, however, a significant temperature difference is captured by the OES spectrum (as shown in Fig. 6). The rotational peaks at 333 nm - 337 nm in the DME/air case are much more pronounced and the temperature difference for two cases is approximately 150 K. Pulse 200 is the point where filamentary structure in the DME/air plasma basically disappears and plasmas return to uniform. From the above data, with repetitive nanosecond pulses, the temperature of plasmas in reactive mixtures will keep increasing, until the ignition event happens. However, there exists a time window where plasma instability is clearly visible.

A phenomenological analysis is performed to estimate the "critical pulse number" for the plasma instability. Physically, when a local quantity (temperature, electron number density etc.) is fluctuated upward and the production rate dominates over the removal rate, this quantity may keep growing locally ("absolute instability") or the fluctuation may transport across the domain ("convective instability"). Such instability dynamics will not stop until a new steady state or a new spatial structure is developed. The thermal-chemical instability in this work develops over millisecond time scales, at which the heat release from plasma reactions or plasma-assisted combustion reactions, and the diffusive/convective heat removal are the major terms for the local thermal balance. In other words, a local point becomes thermally unstable if

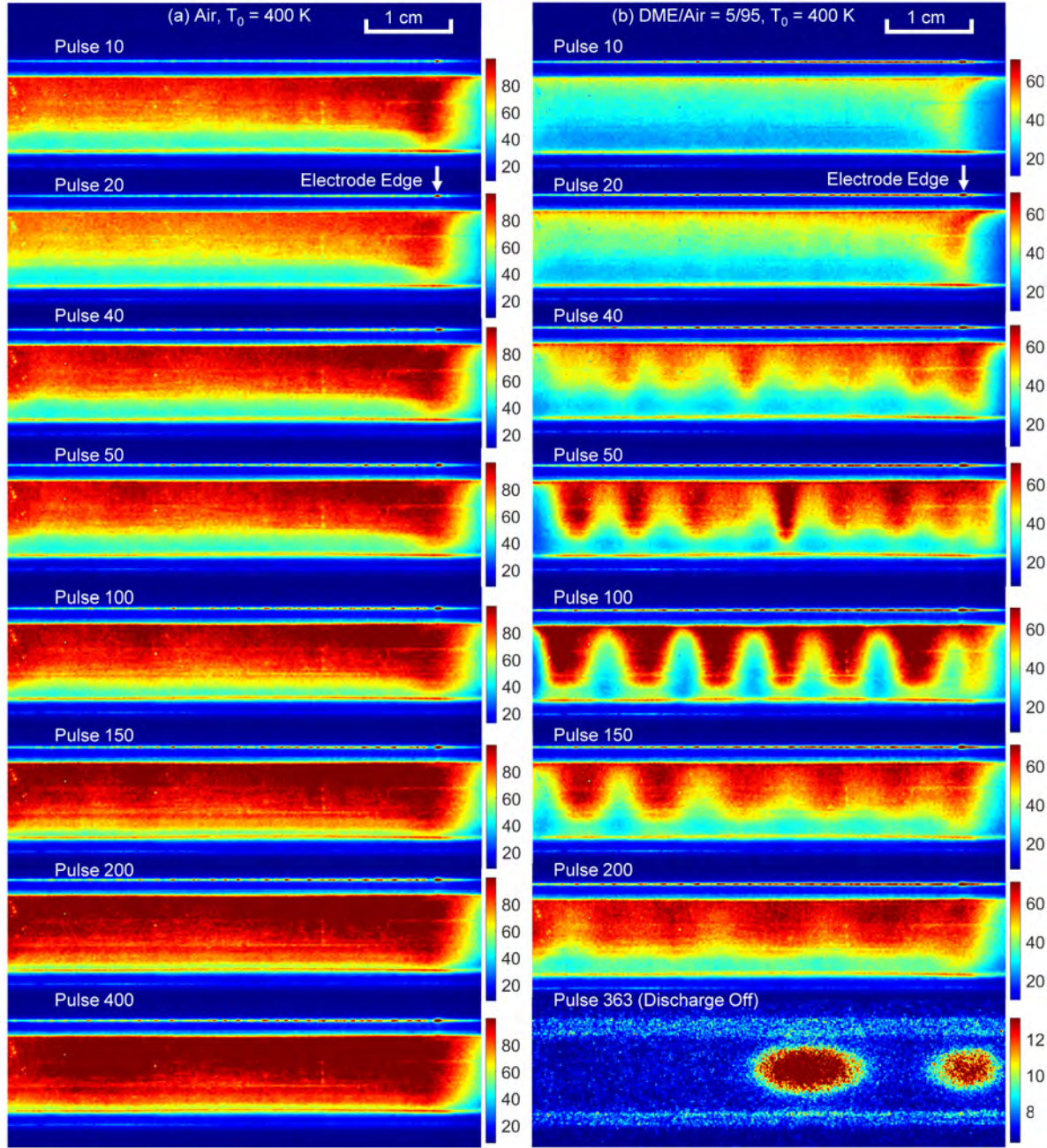$$\dot{Q}_{gen} - \dot{Q}_{loss} > 0 \qquad (11)$$

Figure 5: Single-shot ICCD images of uniform and non-uniform nanosecond pulse discharges in air (first column) and DME-air (second column) at different pulse numbers (labeled above each image). The electrode edge is also labeled. The initial temperature is 400 K. The pulse frequency is 10 kHz. The camera gate is 500 ns for emissions within the pulse ("Discharge On") and 0.2 ms for emissions after the pulse ("Discharge Off").

$\dot{Q}_{gen}$ is the heat release rate, defined as

$$\dot{Q}_{gen} = \dot{Q}_{ext} - \dot{Q}_{chem} - \dot{Q}_{elec} \tag{12}$$

$$= q_{coupled}\nu_{rep} - \sum_{i}^{i_{max}} h_i \frac{\partial N_i}{\partial t} - \frac{3}{2}\frac{\partial(n_e k_B T_e)}{\partial t} \tag{13}$$

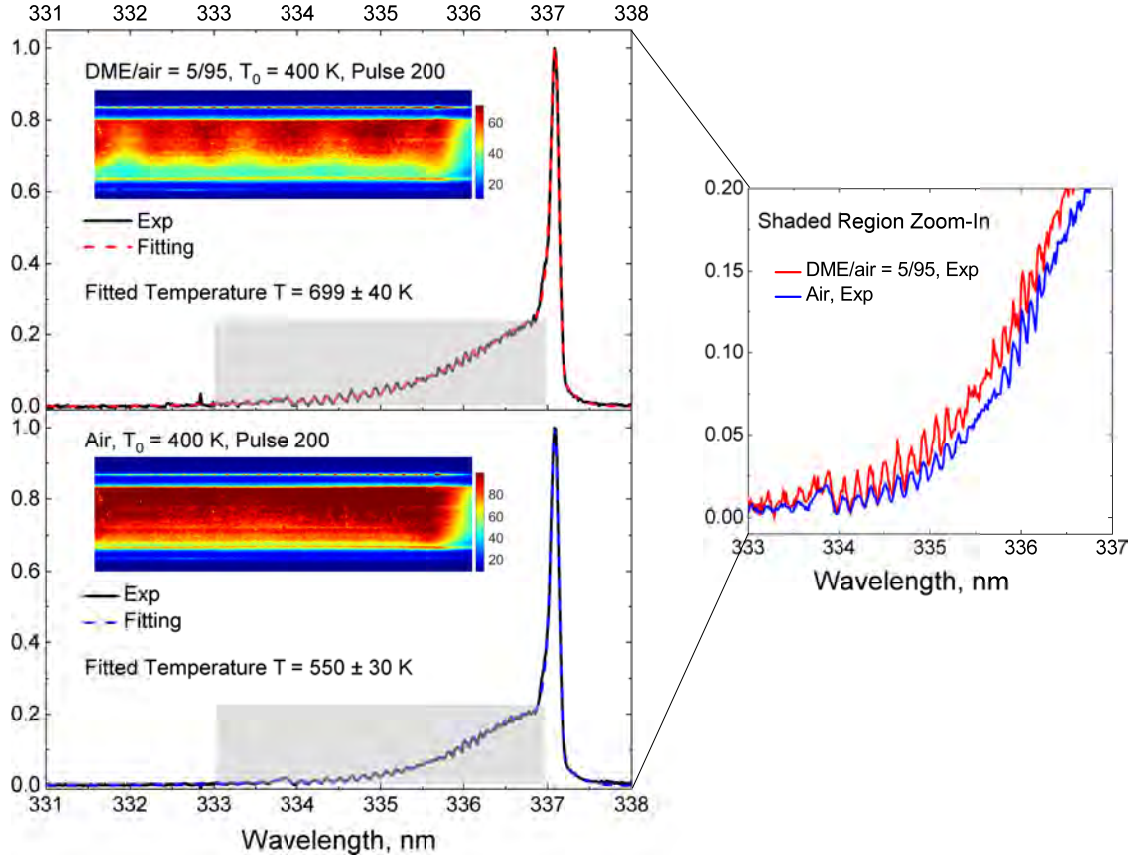*Plasma Thermal-Chemical Instability*   14

Figure 6: Left: Comparisons of experimental and synthetic N_2 emission spectra (second positive band system) of the air and DME-air plasmas at pulse 200. Right: The zoom-in plot of the shaded regions of the spectrum.

From Eqn 13, within the pulse, the discharge energy deposition is considered for calculating $\dot{Q}_{gen}$. In the afterglow phase, $\dot{Q}_{ext} = 0$. Then $\dot{Q}_{gen}$ is from plasma-assisted combustion reactions in reactive flows or from relaxation processes in air. It can be calculated by the zero-dimensional plasma chemistry solver. $\dot{Q}_{loss}$ includes both the heat diffusion and convection, which could be estimated as

$$\dot{Q}_{loss} = \dot{Q}_{diff} + \dot{Q}_{conv}$$

$$\dot{Q}_{diff} = \nabla\left[\lambda(T)\nabla T\right] \approx \lambda(T)\frac{(T - T_0)}{(L/\pi)^2}$$

$$\dot{Q}_{conv} = \rho c_p(T)\mathbf{u}\cdot\nabla T \approx \rho c_p(T)\frac{T - T_0}{\tau_{flow}}$$

The length scale L is 1 cm while τ_{flow} (residence time) is 0.05 s. The dependence of heat capacity $c_p(T)$ and thermal conductivity $\lambda(T)$ on temperature and mixture compositions is considered by using the numerical package [49]. The orders of magnitude of above terms are calculated and plotted in Fig 7.
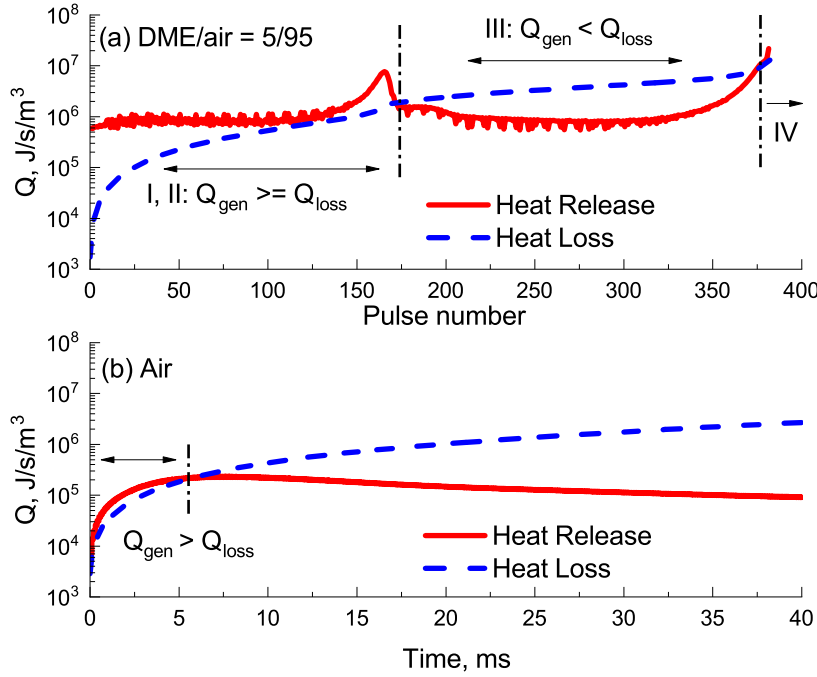
Figure 7: The order of magnitude estimation for $\dot{Q}_{gen}$ and heat loss $\dot{Q}_{loss}$ (both defined in the text) for the (a) DME/air = 5/95 and (b) air mixture. Stage I - IV in (a) are discussed in the text. Note: heat release rate is running-averaged for every pulse.

From Fig 7, in the non-reactive mixture, though the heat release from the fast/slow gas heating provides the initial thermal perturbation, temperature-sensitive heat loss will limit the temperature growth rate and quickly dissipate the plasma instability. The reactive mixture, however, has a much larger heat release rate when activated by the plasma discharge. As a consequence, the dynamics is more complex and can be distinguished into four stages:

- Stage I: Instability initiation. At beginning pulses, though uniformity is still kept in plasma emissions, the local heat release is already orders of magnitude higher than the heat loss.

- Stage II: Thermal overloading. Thin structures with variable intensities are clearly observed in plasma emissions (e.g., Fig 5 Pulse 50, 100). The instability, or the spatial inhomogeneity, keeps growing as the diffusion is fully suppressed by the intense local LTC heat release.

- Stage III: Thermal dissipation. Plasma-enhanced LTC heat release rate reaches a local maximum in Stage II. Then not only heat release rate decreases but the diffusion loss is enhanced at a higher temperature. The filamentary pattern is thermally dissipated with increasing pulses (e.g., Fig 5 Pulse 200).

- Stage IV: Ignition. Once the temperature reaches the ignition threshold, heat release again dominates and the local hot spots transit into ignition kernels.

Plasma Thermal-Chemical Instability   16

The above four-stage dynamics vary with the change of the initial conditions. For example, lowering/increasing the ambient temperature could extend/shorten the time window for Stage II. Highly reactive mixtures may help to skip Stage III and ignition may occur directly from the filaments. More generally, gas-phase or multi-phase additives may change the local thermal balance and shift the instability onset. Surfaces modifications, which may influence the localized surface charges and further the E/N values in the bulk plasma, may also affect the filamentation process.

Back to this work, based on the above analysis and the estimation on the orders of magnitude, for the DME/air mixture (5/95) (Fig. 7(a)), the beginning pulse for observing the plasma instability is within first 40 pulses, where $\dot{Q}_{gen}$ is at least one order of magnitude higher than $\dot{Q}_{loss}$. The ending pulse is pulse 180, after which $\dot{Q}_{loss}$ dominates $\dot{Q}_{gen}$. This prediction is consistent with the ICCD images shown in Fig. 5.

To further validate the hypothesis that plasma instability correlates with the heat release, one can vary the the equivalence ratio from the non-reactive case to the fuel-rich case. From chemistry modeling results in Fig 8, the heat release from the plasma-assisted DME oxidation is delayed from the lean to rich condition. Different from the conventional knowledge in combustion, with plasma discharge, the low-temperature oxidation of fuel-lean mixtures develops faster than that of fuel-rich mixtures. This is due to the active atomic oxygen production by plasma in fuel-lean mixtures. When the DME concentration is higher, more electron energy goes to the DME dissociation channel to generate active radicals. With a larger radical pool and a higher temperature rise, the DME/air plasmas are expected to be less stable.
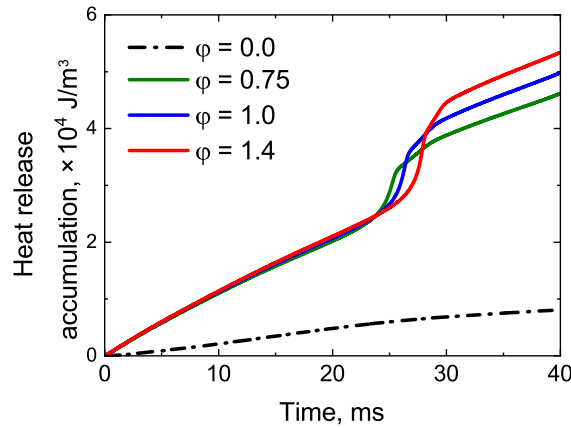

Figure 8: Heat release accumulation under different equivalence ratios. $T_0 = 300$ K. The chemical heat release accumulation is defined as $\int \dot{Q}_{gen} dt$.

The ICCD images and the intensity distribution under the corresponding equivalence ratios are shown in Fig 9. The measurements are made at a lower ambient temperature (300 K), to prevent ignition in all cases. Indeed, with higher DME addition, multiple spatial structures exist at pulse 400, at which the air or the fuel lean mixture nearly returns to quasi-uniform, which is clearly the evidence of the fuel chemistry effect.
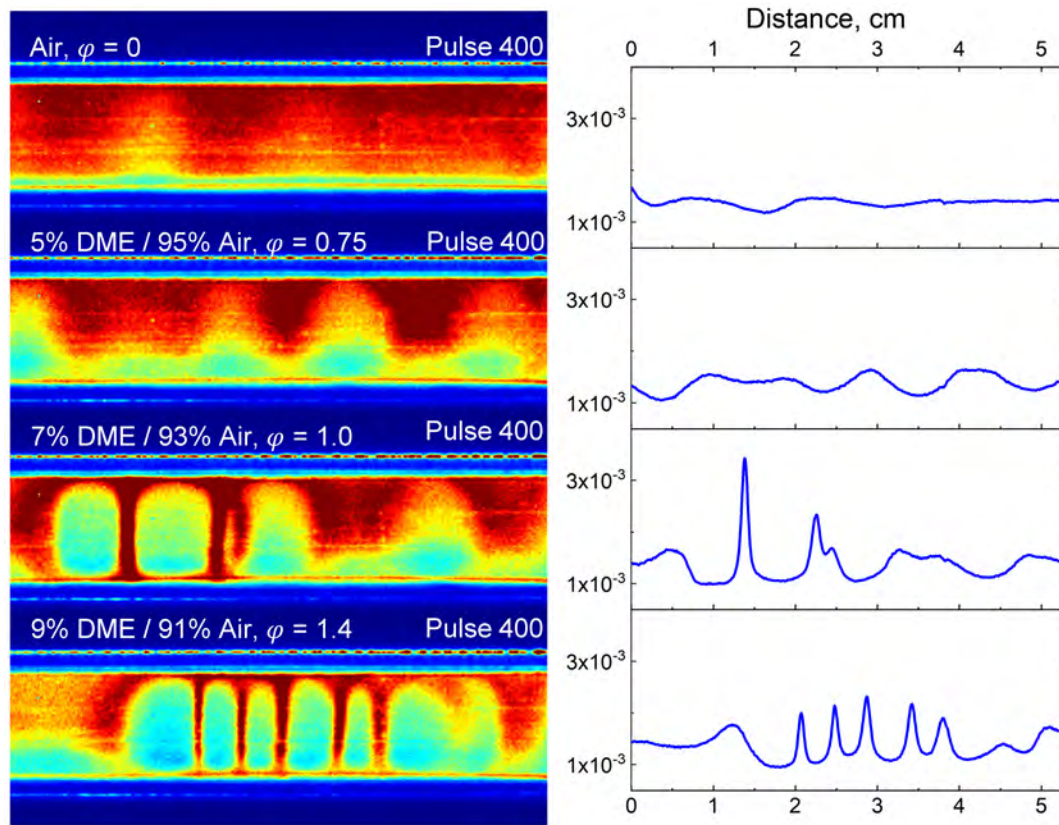
Figure 9: Left: single-shot ICCD images of nanosecond pulse discharges in DME-air mixtures at different equivalence ratios (labeled above each image) at pulse 400. The initial temperature is 300 K. The pulse frequency is 10 kHz. The camera gate is 500 ns for emissions within the pulse ("Discharge On"). Right: Normalized intensity distribution along the stream-wise direction (averaged between the discharge gap).

In summary, single-shot ICCD images in DME/air plasmas clearly demonstrate the dynamics of plasma thermal-chemical instability. Further OES temperature measurements verify the hypothesis that such instability happens with a significant temperature rise. An estimation for the time window of the plasma instability is provided based on a local thermal balance analysis. Additionally, the instability is shown to be amplified or weakened by the variation of the equivalence ratio, which emphasizes the thermal-chemical nature of the observed filamentary structure.

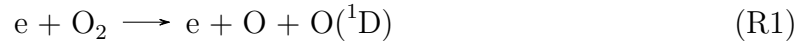### 4.3. Thermal-chemical mode analysis

Chemical heat release is controlled by the underlying chemical kinetics. One fundamental question is: what are the species and reactions most sensitive to the thermal-chemical instability development?
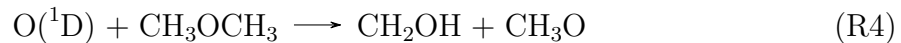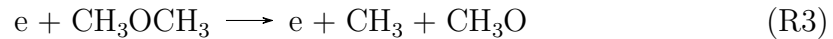
To identify species and reactions controlling the instability, thermal-chemical mode analysis (TCMA) is applied in this work. As indicated by Eqn (9), the stability of

Plasma Thermal-Chemical Instability   18

the chemical source term is determined by the maximum eigenvalue, or the leading TCM. Then for each leading TCM, "explosive mode species/temperature pointer" (SP) is calculated and the representative active species (RAS) will be determined. Due to the unique waveform of the repetitive nanosecond pulsed discharge, the sub-ns/ns kinetic processes would occur within each pulse; the microsecond processes occur between adjacent pulses; and the millisecond processes occur after the accumulation of multiple pulses. Correspondingly, the evolution of eigenvalues in the above time scales present different dynamics.
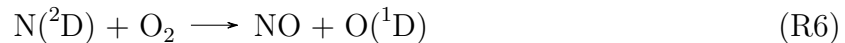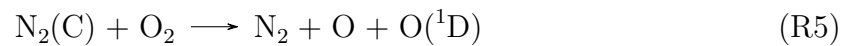
First, within one single pulse (as shown in Fig. 10(a)), the evolution of the maximum eigenvalue closely follows the breakdown process. Table 2 summarizes the detailed information from 1 to 30 ns. For air and DME/air mixtures, the reduced electric field and the temperature rise are similar within such a short time interval. The breakdown happens at approximately 5 - 6 ns. Then the E/N quickly decays. Some non-zero E/N values after the breakdown are caused by the secondary waveform. For unstable thermal-chemical modes, the magnitude of the largest eigenvalues is also similar, ranging from $\mathcal{O}(10^5 \text{ s}^{-1})$ to $\mathcal{O}(10^9 \text{ s}^{-1})$. According to the TCMA analysis, those eigenmodes are mostly connected with the electron-impact and other inelastic reactions, which have a time scale of sub-microseconds ($\mathcal{O}(10^{-9} \text{ s})$ - $\mathcal{O}(10^{-6} \text{ s})$). The RASs for those eigenmodes further confirm this hypothesis. In air, the RASs are the oxygen species for the first 5 ns. The chemical reactions which have the most destabilization effects for the reactive system for the first 5 ns are

$$\text{e} + \text{O}_2 \longrightarrow \text{e} + \text{O} + \text{O}(^1\text{D}) \tag{R1}$$

$$\text{e} + \text{O}_2 \longrightarrow \text{e} + \text{O} + \text{O} \tag{R2}$$

For the DME/air mixture, the most unstable eigenmodes during the breakdown are related to the fuel decomposition. The major pathways are the electron-impact and $\text{O}(^1\text{D})$ reactions as

$$\text{e} + \text{CH}_3\text{OCH}_3 \longrightarrow \text{e} + \text{CH}_3 + \text{CH}_3\text{O} \tag{R3}$$

$$\text{O}(^1\text{D}) + \text{CH}_3\text{OCH}_3 \longrightarrow \text{CH}_2\text{OH} + \text{CH}_3\text{O} \tag{R4}$$

After 5 ns, the TCMA analysis continues pointing to the well-known fast gas heating processes in N_2-O_2 mixture and the NO formation by the quenching the electronically excited species including

$$\text{N}_2(\text{C}) + \text{O}_2 \longrightarrow \text{N}_2 + \text{O} + \text{O}(^1\text{D}) \tag{R5}$$

$$\text{N}(^2\text{D}) + \text{O}_2 \longrightarrow \text{NO} + \text{O}(^1\text{D}) \tag{R6}$$

After nanosecond pulses, the strong perturbation from the discharge disappears and the non-equilibrium species cannot survive. Naturally the unstable TCMs drop by orders of magnitude. Table 3 presents sample TCMA information in the afterglow phase from 11 to 19 ms. Clearly all eigenvalues are at the order of $\mathcal{O}(10^{-1} \text{ s}^{-1})$. The

Plasma Thermal-Chemical Instability 19

Table 2: The list of time (t, unit: ns), largest positive eigenmodes (Re(λ), unit: s^{-1}), and the corresponding representative active species (RAS), the temperature (T, unit: K), and the reduced electric field (E/N, unit: Td) within the first nanosecond pulse. Pressure $p = 100$ Torr. $T_0 = 400$ K.

		Air			DME/Air = 5/95			
t	Re(λ)	RAS	T	E/N	Re(λ)	RAS	T	E/N
1	1.2×10^6	O	400	62	2.8×10^6	CH_3O	400	62
2	1.6×10^7	O	400	119	4.2×10^7	CH_2OH	400	119
3	7.1×10^8	O	400	264	2.7×10^8	CH_2OH	400	264
4	3.4×10^9	O_2	400	425	3.7×10^9	CH_3O_2	400	425
5	6.3×10^9	O	400	536	6.5×10^9	N	400	531
6	6.5×10^5	N_2	400.2	138	9.9×10^6	NO	400.2	82
10	1.4×10^6	O	400.3	0	1.9×10^6	$N_2(C)$	400.3	9
15	1.5×10^5	N_2	400.3	5	1.1×10^6	O_2^*	400.3	2
30	2.2×10^5	NO	400.4	2	6.7×10^5	$N_2(C)$	400.4	2

destabilization effects from the chemical source term are too weak to overcome other damping effects. One example of the damping effects are convection, which has a growth rate of $1/\tau_{flow} \approx \mathcal{O}(10^1 \text{ s}^{-1})$. As a result, it is difficult to have chemical instability in air for this condition.

For DME/air mixtures, the chemistry in the afterglow is different. Without plasma activation, at such a low pressure and low temperature, the TCMs are all stable for the DME/air mixture. The IDT time for the auto-ignition far exceeds the time scale in this work. However, after nanosecond pulses, a radical pool is formed and the unstable TCMs are all activated. In Fig. 10(b), the leading eigenvalues for the DME/air mixture between two adjacent pulses have a transition from $\mathcal{O}(10^4 \text{ s}^{-1})$ down to $\mathcal{O}(10^2 \text{ s}^{-1})$. The major destabilization sources are updated from plasma chemistry to DME low-temperature oxidation chemistry. The chain-branching processes start from CH_3O, CH_3, and CH_3OCH_2. They are major products of DME reactions in the discharge phase (See Table 1). CH_3 can recombine to form ethane, and the following dehydrogenation reactions form C_2H_2. CH_3 can also react with HCO to form acetaldehyde (CH_3CHO). The subsequent reactions of acetaldehyde result in the formation of ketene (CH_2CO). Both C_2H_2 and CH_2CO show up in the RASs shown in Table 3. CH_3OCH_2 goes through the O_2 addition to form $CH_3OCH_2O_2$, which further leads to CH_3OCH_2O or $O_2CH_2OCH_2O_2H$. The above kinetics now control the unstable chemical modes in a temperature range of 550 - 800 K. Such a temperature range and its millisecond time scale matches well with the "thermal overloading" and " thermal dissipation" stage of plasma instability (discussed in Section 4.2). Path flux analysis (PFA), which integrates the reaction rates over different pulses until the ignition, further confirms that the

Plasma Thermal-Chemical Instability   20

low-temperature chemical reactions are the major flux connecting major species in the afterglow stage (shown in Fig. 11).

Table 3: The list of time (t, unit: ms), largest positive eigenmodes (Re(λ), unit: s^{-1}), and the corresponding representative active species (RAS), the temperature (T, unit: K) in the afterglow phase in the DME/air first-stage ignition (Temperature range: 550 - 800 K). Pressure p = 100 Torr. T_0 = 400 K.

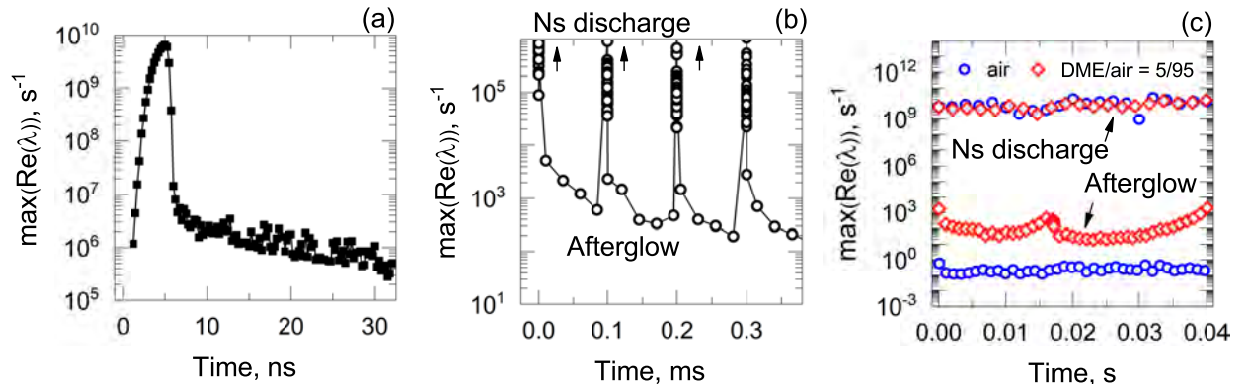|		Air		DME/Air = 5/95		
t	Re(λ)	RAS	T	Re(λ)	RAS	T
11	3.9×10^{-1}	O_2	462	5.5×10^{1}	CH_3OCH_2	543
12	1.0×10^{-1}	N_2	469	6.2×10^{1}	C_2H_2	551
13	2.1×10^{-1}	O	476	8.7×10^{1}	CH_3CO	567
14	2.5×10^{-1}	O_2	485	1.5×10^{2}	CH_2CO	582
15	3.4×10^{-1}	O_2	493	2.4×10^{2}	H	602
16	1.6×10^{-1}	N_2	502	4.0×10^{2}	H	625
17	1.7×10^{-1}	O_2	510	1.8×10^{2}	$O_2CH_2OCH_2O_2H$	702
18	2.2×10^{-1}	O	519	3.9×10^{1}	CH_3OCH_2	739
19	2.5×10^{-1}	O	528	3.4×10^{1}	CH_3OCH_2O	766

Figure 10: Evolution of the eigenvalues for the leading thermal-chemical modes (a) within a nanosecond pulse (DME/air = 5/95). (b) between individual nanosecond pulses (DME/air = 5/95) (c) in the millisecond time scales (DME/air = 5/95 and air). p = 100 Torr. T_0 = 400K.

To conclude the discussion of TCMA analysis, we plot the leading eigenvalues in the nanosecond pulse phase and the afterglow phase in Fig. 10(c). The "transitional" eigenvalues between those two phases are not presented for clarity. Fig. 10(c) provides a comprehensive picture of how unstable thermal-chemical modes evolve in different pulses of a nanosecond repetitively pulsed discharge. For both reactive and non-reactive cases, before every breakdown, unstable TCMs with eigenvalues of $\mathcal{O}(10^9 \text{ s}^{-1})$ exist following
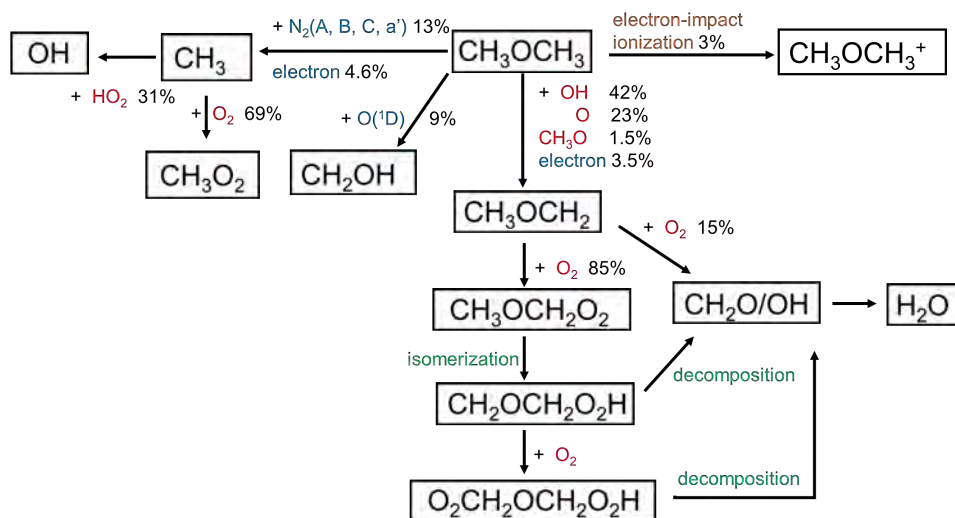
Figure 11: Path flux analysis (PFA) in DME/air mixture in the time-dependent simulations.

the discharge physics at the nanosecond time scale. However, between adjacent pulses, air chemistry can only provide much weaker unstable TCMs compared to the DME oxidation chemistry. The fingerprints of two-stage DME oxidation at low temperature are clearly observed in the figure. Such fast destabilization effects from chemistry further promote the local heat release and trigger the plasma thermal-chemical instability.

5. Conclusion

In this work, plasma thermal-chemical instability triggered by DME low temperature oxidation in repetitive nanosecond pulsed DBD discharge is investigated from the perspective of experimental measurements and theoretical analysis. First, DME low-temperature heat release plays a key role in promoting the plasma instability. A significant temperature difference ($\sim \mathcal{O}(10^2 \text{ K})$) is observed between the air plasmas and DME-air plasmas given the same number of pulses. Second, the instability development has a multi-stage dynamics: With an increasing of pulse numbers, the well-defined structures develop from initially uniform plasmas. Filaments further dissipate and the plasma returns to the uniform state because the local heat release is weakened after the DME first-stage ignition and the thermal diffusion is promoted with elevated temperature. Once the temperature reaches the ignition threshold, plasma-assisted ignition will occur. It is also shown that different from the conventional knowledge in combustion, with plasma discharge, the low-temperature oxidation of a fuel-lean mixture could develop faster than that of a fuel-rich mixture. This is mainly controlled by the active atomic oxygen production by plasma in the fuel-lean mixture. Lastly, thermal-chemical mode analysis (TCMA) is used to link the instability dynamics with unstable thermal-chemical modes. Due to the intrinsic multi-scale feature of the

Plasma Thermal-Chemical Instability   22

repetitive nanosecond pulsed discharges, the leading thermal-chemical modes vary by orders of magnitude in the discharge and afterglow phase. DME low-temperature oxidation chemistry, instead of the discharge physics or chemistry at the nanosecond time scale, is the dominant factor for destabilizing the plasma. A better understanding of the chemical origin of such instability will provide more guidance for chemical manufacturing and energy conversion applications based on non-equilibrium plasma discharges. Future work includes diagnostics and manipulation of plasma uniformity in endothermic mixtures (e.g. ammonia mixtures), multi-phase flows (e.g. spray and aerosols) and catalytic systems.

Acknowledgments

REFERENCES   23

References

[1] A Bogaerts, X Tu, J C Whitehead, G Centi, L Lefferts, O Guaitella, F Azzolina-Jury, H Kim, A B Murphy, W F Schneider, et al. The 2020 plasma catalysis roadmap. *Journal of Physics D: Applied Physics*, 53(44):443001, 2020.

[2] I Adamovich, S D Baalrud, A Bogaerts, P J Bruggeman, M Cappelli, V Colombo, U Czarnetzki, U Ebert, J G Eden, P Favia, et al. The 2017 plasma roadmap: Low temperature plasma science and technology. *Journal of Physics D: Applied Physics*, 50(32):323001, 2017.

[3] Y Ju and W Sun. Plasma assisted combustion: dynamics and chemistry. *Progress in Energy and Combustion Science*, 48:21–83, 2015.

[4] I V Adamovich and W R Lempert. Challenges in understanding and predictive model development of plasma-assisted combustion. *Plasma Physics and Controlled Fusion*, 57(1):014001, 2014.

[5] X Mao, H Zhong, Z Wang, T Ombrello, and Y Ju. Effects of inter-pulse coupling on nanosecond pulsed high frequency discharge ignition in a flowing mixture. *Proceedings of the Combustion Institute*, 2023.

[6] X Mao, H Zhong, T Zhang, A Starikovskiy, and Y Ju. Modeling of the effects of non-equilibrium excitation and electrode geometry on h2/air ignition in a nanosecond plasma discharge. *Combustion and Flame*, 240:112046, 2022.

[7] G Ecker, W Kröll, and O Zöller. Thermal instability of the plasma column. *The Physics of Fluids*, 7(12), 1964.

[8] R A Haas. Plasma stability of electric discharges in molecular gases. *Physical Review A*, 8(2):1017, 1973.

[9] Y P Raizer. *Gas discharge physics*. Springer, 1991.

[10] A V Eletskii and B M Smirnov. Nonuniform gas discharge plasma. *Physics-Uspekhi*, 39(11):1137, 1996.

[11] H Zhong, M N Shneider, M S Mokrov, and Y Ju. Thermal-chemical instability of weakly ionized plasma in a reactive flow. *Journal of Physics D: Applied Physics*, 2019.

[12] H Zhong, M N Shneider, X Mao, and Y Ju. Dynamics and chemical mode analysis of plasma thermal-chemical instability. *Plasma Sources Science and Technology*, 30(3):035002, 2021.

[13] A C Rousso, B M Goldberg, T Y Chen, S Wu, A Dogariu, R B Miles, E Kolemen, and Y Ju. Time and space resolved diagnostics for plasma thermal-chemical instability of fuel oxidation in nanosecond plasma discharges. *Plasma Sources Science and Technology*, 2020.

[14] I Choi, M Uddi, N Jiang, I Adamovich, and W Lempert. Stability and heating rate of air and ethylene-air plasmas sustained by repetitive nanosecond pulses. In *47th AIAA Aerospace Sciences Meeting*, page 688, 2009.

REFERENCES 24

[15] H Zhong, X Mao, A C Rousso, C L Patrick, C Yan, W Xu, Q Chen, G Wysocki, and Y Ju. Kinetic study of plasma-assisted n-dodecane/O_2/N_2 pyrolysis and oxidation in a nanosecond-pulsed discharge. *Proceedings of the Combustion Institute*, 2020.

[16] Aric Rousso, Xingqian Mao, Qi Chen, and Yiguang Ju. Kinetic studies and mechanism development of plasma assisted pentane combustion. *Proceedings of the Combustion Institute*, 37(4):5595–5603, 2019.

[17] Z Yin, K Takashima, and I V Adamovich. Ignition time measurements in repetitive nanosecond pulse hydrogen-air plasmas at elevated initial temperatures. *IEEE Transactions on Plasma Science*, 39(12):3269–3282, 2011.

[18] Z Yin, A Montello, C D Carter, W R Lempert, and I V Adamovich. Measurements of temperature and hydroxyl radical generation/decay in lean fuel-air mixtures excited by a repetitively pulsed nanosecond discharge. *Combustion and Flame*, 160(9):1594–1608, 2013.

[19] Z Yin. *Fuel Oxidation and Ignition by Nanosecond Pulse Discharges at Elevated Temperatures*. The Ohio State University, 2013.

[20] A C Rousso. *Plasma-assisted Combustion: Kinetics and Control*. PhD thesis, Princeton University, 2019.

[21] A J Wolf, T W H Righart, F J J Peeters, W A Bongers, and M C M van de Sanden. Implications of thermo-chemical instability on the contracted modes in CO_2 microwave plasmas. *Plasma Sources Science and Technology*, 29(2):025005, 2020.

[22] P Viegas, L Vialetto, A J Wolf, F Peeters, P W C Groen, T H Righart, W Bongers, R Van de Sanden, and P Diomede. Insight into contraction dynamics of microwave plasmas for CO_2 conversion from plasma chemistry modelling. *Plasma Sources Science and Technology*, 2020.

[23] S Kelly, A van de Steeg, A Hughes, G van Rooij, and A Bogaerts. Thermal instability and volume contraction in a pulsed microwave N_2 plasma at sub-atmospheric pressure. *Plasma Sources Science and Technology*, 30(5):055005, 2021.

[24] A Starikovskiy, M N Shneider, D Marinov, and S Starikovskaya. Thermal ionization instability development in air plasma generated by repetitive ns dielectric barrier discharge. In *52nd Aerospace Sciences Meeting*, page 1031, 2014.

[25] W Sun, S H Won, and Y Ju. In situ plasma activated low temperature chemistry and the s-curve transition in DME/oxygen/helium mixture. *Combustion and Flame*, 161(8):2054–2063, 2014.

[26] R Zhang, H Liao, J Yang, and B Yang. Exploring chemical kinetics of plasma assisted oxidation of dimethyl ether (DME). *Combustion and Flame*, 225:388–394, 2021.

[27] V Gururajan and F N Egolfopoulos. Transient plasma effects on the autoignition of DME/O_2/Ar and C_3H_8/O_2/Ar mixtures. *Proceedings of the Combustion Institute*, 36(3):4165–4174, 2017.

REFERENCES   25

[28] Z Zhao, M Chaos, A Kazakov, and F L Dryer. Thermal decomposition reaction and a comprehensive kinetic model of dimethyl ether. *International Journal of Chemical Kinetics*, 40(1):1–18, 2008.

[29] C B Reuter, S H Won, and Y Ju. Experimental study of the dynamics and structure of self-sustaining premixed cool flames using a counterflow burner. *Combustion and Flame*, 166:125–132, 2016.

[30] E A Filimonova. Discharge effect on the negative temperature coefficient behaviour and multistage ignition in C_3H_8-air mixture. *Journal of Physics D: Applied Physics*, 48(1):015201, 2014.

[31] I N Kosarev, S V Kindysheva, I V Kochetov, A Y Starikovskiy, and N L Aleksandrov. Shock-tube study of dimethyl ether ignition by high-voltage nanosecond discharge. *Combustion and Flame*, 203:72–82, 2019.

[32] S Yang, S Nagaraja, W Sun, and V Yang. Multiscale modeling and general theory of non-equilibrium plasma-assisted ignition and combustion. *Journal of Physics D: Applied Physics*, 50(43):433001, 2017.

[33] A Bao, Y G Utkin, S Keshav, G Lou, and I V Adamovich. Ignition of ethylene–air and methane–air flows by low-temperature repetitively pulsed nanosecond discharge plasma. *IEEE Transactions on Plasma Science*, 35(6):1628–1638, 2007.

[34] P J Bruggeman, N Sadeghi, D C Schram, and V Linss. Gas temperature determination from rotational lines in non-equilibrium plasmas: a review. *Plasma Sources Science and Technology*, 23(2):023001, 2014.

[35] X Yang, E Jans, C Richards, S Raskar, D van den Bekerom, K Wu, and I V Adamovich. Measurements of atoms and metastable species in n2 and h2–n2 nanosecond pulse plasmas. *Plasma Sources Science and Technology*, 31(1):015017, 2022.

[36] I V Adamovich, M Nishihara, I Choi, M Uddi, and W R Lempert. Energy coupling to the plasma in repetitive nanosecond pulse discharges. *Physics of Plasmas*, 16(11):113505, 2009.

[37] Y P Raizer and M N Shneider. Electrodeless capacitive discharge sustained by repetitive high-voltage pulses. *High Temperature*, 27(3):329–335, 1989.

[38] S Pancheshnyi, B Eismann, G J M Hagelaar, and L C Pitchford. Computer code zdplaskin. *University of Toulouse, LAPLACE, CNRS-UPS-INP, Toulouse, France*, 2008.

[39] A E Lutz, R J Kee, and J A Miller. Senkin: A fortran program for predicting homogeneous gas phase chemical kinetics with sensitivity analysis. Technical report, Sandia National Labs., Livermore, CA (USA), 1988.

[40] Xingqian Mao, Aric Rousso, Qi Chen, and Yiguang Ju. Numerical modeling of ignition enhancement of $CH_4/O_2/He$ mixtures using a hybrid repetitive nanosecond and dc discharge. *Proceedings of the Combustion Institute*, 37(4):5545–5552, 2019.

REFERENCES   26

[41] Xingqian Mao, Qi Chen, Aric C Rousso, Timothy Y Chen, and Yiguang Ju. Effects of controlled non-equilibrium excitation on $H_2/O_2/He$ ignition using a hybrid repetitive nanosecond and dc discharge. *Combustion and Flame*, 206:522–535, 2019.

[42] G J M Hagelaar and L C Pitchford. Solving the boltzmann equation to obtain electron transport coefficients and rate coefficients for fluid models. *Plasma Sources Science and Technology*, 14(4):722, 2005.

[43] S Pancheshnyi, S Biagi, M C Bordage, G J M Hagelaar, W L Morgan, A V Phelps, and L C Pitchford. The lxcat project: electron scattering cross sections and swarm parameters for low temperature plasma modeling. *Chemical Physics*, 398:148–153, 2012.

[44] S Biagi. Magboltz, program to compute gas transport parameters. *Version*, 11, 1997.

[45] H Zhao, X Yang, and Y Ju. Kinetic studies of ozone assisted low temperature oxidation of dimethyl ether in a flow reactor using molecular-beam mass spectrometry. *Combustion and Flame*, 173:187–194, 2016.

[46] C Yan, H Zhao, Z Wang, G Song, Y Lin, C R Mulvihill, A W Jasper, S J Klippenstein, and Y Ju. Low-and intermediate-temperature oxidation of dimethyl ether up to 100 atm in a supercritical pressure jet-stirred reactor. *Combustion and Flame*, page 112059, 2022.

[47] K P Shrestha, S Eckart, A M Elbaz, B R Giri, C Fritsche, L Seidel, W L Roberts, H Krause, and F Mauss. A comprehensive kinetic model for dimethyl ether and dimethoxymethane oxidation and NOx interaction utilizing experimental laminar flame speed measurements at elevated pressure and temperature. *Combustion and Flame*, 218:57–74, 2020.

[48] S H Lam and D A Goussis. Understanding complex chemical kinetics with computational singular perturbation. In *Symposium (International) on Combustion*, volume 22, pages 931–941. Elsevier, 1989.

[49] R J Kee, G Dixon-Lewis, J Warnatz, M E Coltrin, and J A Miller. A fortran computer code package for the evaluation of gas-phase multicomponent transport properties. Technical report, Sandia National Labs., Livermore, CA (USA), 1986.